Continuum mechanics at the atomic scale

Solhjoo, Soheil; Vakis, Antonis I.

Published in:
Journal of Applied Physics

DOI:
10.1063/1.4967795

Continuum mechanics at the atomic scale: Insights into non-adhesive contacts using molecular dynamics simulations

Soheil Solhjoo, and Antonis I. Vakis

Citation: Journal of Applied Physics **120**, 215102 (2016); doi: 10.1063/1.4967795
View online: https://doi.org/10.1063/1.4967795
View Table of Contents: http://aip.scitation.org/toc/jap/120/21
Published by the American Institute of Physics

Continuum mechanics at the atomic scale: Insights into non-adhesive contacts using molecular dynamics simulations

Soheil Solhjoo and Antonis I. Vakis[a)]
Advanced Production Engineering, Engineering and Technology Institute Groningen, Faculty of Mathematics and Natural Sciences, University of Groningen, Nijenborg 4, 9747 AG Groningen, The Netherlands

(Received 28 July 2016; accepted 1 November 2016; published online 1 December 2016)

Classical molecular dynamics (MD) simulations were performed to study non-adhesive contact at the atomic scale. Starting from the case of Hertzian contact, it was found that the reduced Young's modulus E^* for shallow indentations scales as a function of, both, the indentation depth and the contact radius. Furthermore, the contact of two representative rough surfaces was investigated: one multi-asperity, Greenwood-Williamson-type (GW-type) rough surface — where asperities were approximated as spherical caps — and a comparable randomly rough one. The results of the MD simulations were in agreement for both representations and showed that the relative projected contact areas A_{rpc} were linear functions of nominal applied pressures, even after the initiation of plastic deformation. When comparing the MD simulation results with the corresponding continuum GW and Persson models, both continuum models were found to overestimate the values of A_{rpc} relative to the MD simulation results. *Published by AIP Publishing.*
[http://dx.doi.org/10.1063/1.4967795]

I. INTRODUCTION

One of the most important factors investigated in tribological studies is the real contact area A_{real}, which is typically much smaller than the nominal contact area A_0, due to the roughness of the contacting surfaces. In macroscopic experiments, the real contact area can be usually described as $A_{real} = F_f/\bar{\tau}$, where F_f is the friction force and $\bar{\tau}$ is the effective shear strength of the contacting bodies. On the other hand, in continuum contact mechanics models, the contact area is typically defined as a function of separation, normal force, or nominal pressure. While such continuum models were developed for macroscopic contacts, advancements in nano-sized devices required researchers to extend continuum theories to the nanoscale. Nevertheless, the atomic resolution of nano-contacts with its inherently discrete nature goes against one of the essential assumptions of continuum theories, namely, that the contacting surfaces are continuous. This problem led researchers to study nano- contacts by means of atomistic computer simulation methods, such as molecular dynamics (MD).

MD simulations have been used to describe the contact behavior at different situations: normal or sliding contacts, flat or rough surfaces, with or without adhesion, with or without lubricant, and so on.[1–6] Some researchers went further to compare their simulation results with relevant continuum models; however, discrepancies between the two resulted in a number of extensions to continuum models such as developing an extended version of the Johnson-Kendall-Roberts (JKR) theory[7,8] and proposing a three-parameter friction law.[9] In a detailed investigation by Luan and Robbins, the breakdown of continuum models for mechanical contact at the atomic scale was demonstrated[10] to be due to the inherent atomic roughness at the contacts; however, Mo *et al.*[11] later argued that the definition of the real contact area needs to be corrected for the atomic scale, which will result in comparable results with the relevant continuum models. They defined the real contact area as $A_{real} = N_{ca}A_a$, where N_{ca} is the number of contacting atoms and A_a is the projected area of an individual atom. Solhjoo and Vakis[12] further investigated different methods for identifying the contacting atoms and argued that the most suitable method for doing so is based on atomic distances, i.e., two atoms are identified as being in contact if their pair-distance is closer than a contact distance d_c. Moreover, they showed that $g(r)$ curves, depicting the normalized radial distribution function of the system, can be used to define this contact distance as well as the diameter of an individual atom in an adhesive contact.

While the definition of the adhesive contact distance was investigated in detail previously,[12] the non-adhesive contact distance is not well defined but is very relevant in direct comparisons between atomistic simulations and non-adhesive classical continuum theories. An atom can be identified as being in contact if it is acted upon by a non-zero force from the counterpart.[12] This force-based definition can be translated into a distance-based one in which the governing potential energy needs to be considered. While such definitions have been widely adopted, there is a lack of validating investigations, especially with regard to widely accepted continuum theories.

In this work, non-adhesive contacts were studied by means of classical MD simulations, and the results were analyzed and compared with relevant continuum models. First, a number of single asperity contacts were investigated, which resulted in a differentiation between the definitions of interacting and contacting atoms. Moreover, through analyzing the results in the context of continuum contact mechanics models, it was shown that, for indentations exceeding a finite

[a)]Author to whom correspondence should be addressed. Electronic mail: a.vakis@rug.nl. Tel.: +31 50 363 4202.

indentation depth, the mechanical behavior of the contact tends to that described by the continuum theories studied in this paper. Furthermore, two types of rough surface contacts were simulated, building on the single asperity contact investigation. The results showed that the simulation predictions are comparable to those of continuum models.

II. A SHORT REVIEW ON NON-ADHESIVE CONTACT MECHANICS

Different models have been developed for analyzing non-adhesive contact mechanics, which share some common assumptions: the surfaces are continuous and smooth, each solid can be considered as an elastic half-space, and the strains are small for elasticity to be valid.[13] Moreover, most of the models assume frictionless contact.

The first successful model for analyzing non-adhesive contacts between two solids was published by Hertz[14] (see, e.g., Ref. 13 for a review). This model was later adapted and made applicable to adhesive contacts as well, e.g., in the classical JKR[7] and Derjaguin-Muller-Toporov (DMT)[15] theories. Furthermore, the Hertz theory was utilized by Greenwood and Williamson (GW)[16] in their well-known study of rough surface contact, while a "competing" contact mechanics model of rough surfaces was introduced and further developed by Persson;[17,18] the applicability and limitations of the GW-inspired and Persson models are still debated.[19] In the present work, atomistic systems corresponding to the Hertz, GW, and Persson models are examined in order to investigate the applicability of these models, which were originally developed for continuum mechanics, to atomistic contacts.

A. The Hertz model

Hertz analytically solved the contact mechanics problem of elliptical point contacts.[14] Assuming the same values of principle radii of curvature for each surface, the area of contact will be circular; therefore, the two contacting surfaces have two radii of curvature of R_1 and R_2, and $R = (R_1^{-1} + R_2^{-1})^{-1}$ would be the relative radius of contact. For such a contact, Hertz proposed a pressure distribution of the form $p(r) = p_0(1 - (r/r_c)^2)^{0.5}$, where r is the radial distance of the contact (with 0 at the center of the contact), p_0 is the maximum compressive pressure, and r_c is the radius of the contact area projected on a plane normal to the applied load. The proposed pressure distribution results in the following relations:

$$r_c = \left(\frac{3F_\perp R}{4E^*}\right)^{1/3} \tag{1}$$

and

$$p_0 = \left(\frac{6F_\perp E^{*2}}{\pi^3 R^2}\right)^{1/3} \tag{2}$$

with

$$E^* = \left(\frac{1-\nu_1^2}{E_1} + \frac{1-\nu_2^2}{E_2}\right)^{-1}, \tag{3}$$

where $F_\perp$ is the normal applied force, and E_i and ν_i are the elastic modulus and the Poisson ratio of the contacting bodies. Moreover, the normal applied force relates to the indentation depth via $F_H = \frac{4}{3}E^* R^{0.5} d^{1.5}$.

B. The GW model

Greenwood and Williamson analyzed the non-adhesive contact between rough surfaces by applying Hertzian theory.[16] In their model, the contact of two rough surfaces was simplified as one equivalent elastic rough surface contacting a rigid flat, under the assumption that the final rough surface has an isotropic normal height distribution. Then, they modelled the rough surface as a distribution of N asperities having spherical caps with a constant radius. Their original model was developed for non-adhesive and elastic contacts and ignored all types of interactions between the asperities. At any given separation s, defined as the distance between the rigid surface and the mean value of the asperity heights, the GW model describes the projected contact area A_{GW} and the contact normal force F_{GW} as functions of separation as follows:

$$A_{GW} = N \int_s^\infty A_H(h-s)P(h)\,\mathrm{d}h \tag{4}$$

and

$$F_{GW} = N \int_s^\infty F_H(h-s)P(h)\,\mathrm{d}h, \tag{5}$$

where h is the asperity height, A_H and F_H are the projected contact area and the normal compressive force of each asperity, respectively, calculated from the Hertz model, and $P(h)$ is the height distribution.

C. The Persson model

Persson developed a multiscale contact theory by applying a diffusion-like formula to implement scale dependency to his model, which relates the projected contact area of a rigid rough surface contacting an elastic flat surface to the applied pressure.[17,18] The theory was originally developed for non-adhesive contacts, where the rough surface is a quasi self-affine one with an isotropic and normal height distribution. Before the description of the model, let us define the relative projected contact area ratio as $A_{rpc} = A_{pc}/A_0$, where A_{pc} is the projection of the real contact area on a plane normal to the applied load, and is not to be confused with the area A_H calculated from the Hertz model, and A_0 is the apparent contact area, i.e., $L_x \times L_y$, where L_x and L_y are the lateral lengths of the contacting system.

In this theory, the projected contact area $A_{Persson}$ is a function of an arbitrary length scale λ, assuming that the original surface is smooth at all length scales below λ.[20] This

length scale is defined as $\lambda = L/\zeta$, where ζ is called the "magnification level," and $\zeta \geq 1$. The magnification level controls the length scale λ, so that λ is the shortest wavelength of roughness that can be resolved at magnification ζ.[21] Although, in theory, the value of λ is bounded by the distance between two neighboring atoms, in practice its value cannot be smaller than the lateral resolution of scanning instruments.

In an elastic contact, the relative projected contact area at a given magnification is defined as $A_{rpc} = \int_0^\infty P(p)dp$, where p is the interfacial contact pressure and $P(p)$ is the probability distribution of p. Persson solved his proposed diffusion-like model, which resulted in the normalized area of real contact

$$A_{rpc} = \mathrm{erf}\left(\frac{P_0}{2\sqrt{G}}\right) \tag{6}$$

with $P_0 = F_\perp/A_0$. Parameter G was obtained, both, analytically[17,18] and numerically.[21] Figure 1 shows a typical power spectral density (PSD) of a quasi self-affine rough surface. For such surfaces, the value of G can be calculated from the power spectral density of the surface (PSD), in the form of

$$G = \frac{\pi}{4}E^{*2}\int_{q_L}^{\zeta q_L} q^3 C(q)dq, \tag{7}$$

where $C(q)$ is the PSD of the surface and q is the wavenumber. Note that $\zeta q_L \leq q_H$, where $q_L = 2\pi/L$ and $q_H = 2\pi/2\delta$ are the smallest and largest wavenumbers of the PSD, with δ being the shortest distance between two sampled neighboring point. Comparing Eq. (7) with the second moment of the PSD, it can be shown that $G = \frac{1}{8}E^{*2}\langle|\nabla h|^2\rangle$ (e.g., see Refs. 22 and 23), where $\langle|\nabla h|^2\rangle$ is the mean square gradient of the surface. It should be noted that the values of G and $\langle|\nabla h|^2\rangle$ are dependent on the magnification level ζ.

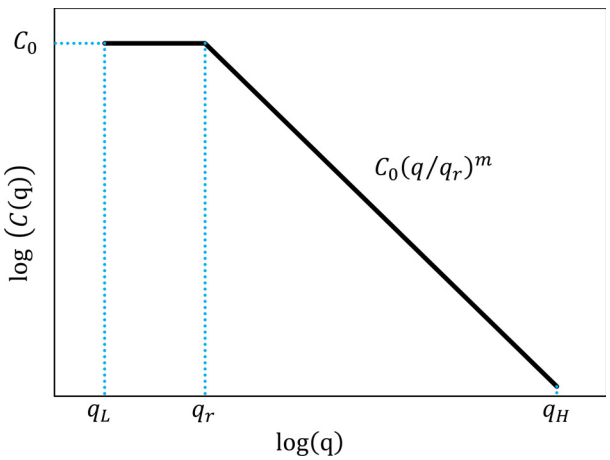

FIG. 1. The schematic power spectral density of a quasi self-affine rough surface with an isotropic height distribution: C_0 is a constant, $q_L = 2\pi/L$ and $q_L = 2\pi/\delta$ are the smallest and largest wave numbers, and q_r is the roll-off wavenumber. Note that the scales are logarithmic.

The numerical approach was based on the fitting of a double Gaussian function of the following form to the interfacial stress distribution:

$$P(p) = \frac{1}{2\sqrt{\pi\bar{G}}}\left(\exp\left(-\frac{(p-P_0)^2}{4\bar{G}}\right) - \exp\left(-\frac{(p+P_0)^2}{4\bar{G}}\right)\right). \tag{8}$$

Theoretically, $G = \bar{G}$; however, it was shown that the ratio $r = \bar{G}/G$ varies between 0.5 and 1, i.e., the theoretical solution requires a correction factor.[24]

III. SIMULATION METHODOLOGY

A. Overview of numerical experiments

In order to examine the applicability of the Hertz, GW, and Persson contact models at the atomic scale, three different systems had to be simulated separately: in the first one, a single asperity comes into contact with a flat substrate; in the other two, a flat substrate touches a multi-asperity rough surface and a randomly rough surface, respectively. Each of the systems was comprised of a rigid indenter, in the form of a single asperity or a rough surface, and a deformable counterpart constructed from three different layers: (1) the two atomic layers farthest from the contact were fixed to resemble a rigid substrate and provide the needed support, (2) the next four atomic layers were assigned to be the thermostatic layer, and (3) the remaining atoms were Newtonian and formed the free layer. The various studied systems are summarized in Table I. Although the geometrical structure of the systems was different in each case, all other parameters were the same in all simulations.

The large-scale atomic/molecular massively parallel simulator (LAMMPS) was used to carry out the simulations.[25] Applying a step size of 10 fs,[26] the equations of motion were solved via the velocity-Verlet algorithm.[27] The temperature of the thermostatic layers was set to 300 K using Berendsen's thermostat.[28] The systems were equilibrated before the initiation of contact for ~0.5 ns. Moreover, in order to overcome the thermal fluctuations,[29] the forces and pressure values were collected by averaging the values over 0.1 ps and 10 ps, respectively. The crystalline direction of [111] was defined as the z coordinate direction. Periodic boundary conditions were applied along the lateral directions. The post processing analyses were done by means of OVITO,[30] ImageJ,[31] and a number of codes written explicitly for this purpose in MATLAB (The MathWorks, Inc., Natick, MA).

B. Potential energies

All of the systems in this investigation were generated of calcium with FCC crystal structure and a lattice parameter of $a_0 = 5.5884$ Å.[32] Two different types of potential energies were used in this study: one for the atoms of the deformable blocks, and one for the interactions between the counterparts. The atoms of each block were governed by the embedded atom method (EAM) potential[33] with the database developed by Sheng *et al.* for calcium.[32] In order to replicate a non-

TABLE I. A summary of the different types of the simulated systems in this work, and their placement in the results and discussion section.

System type	System snapshot	Placement in the text
Single asperity contact	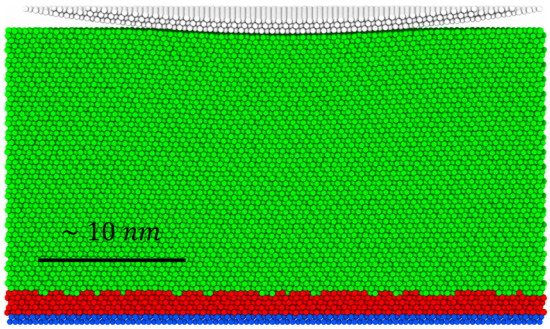	IV A. Single asperity contact size effects
GW rough contact	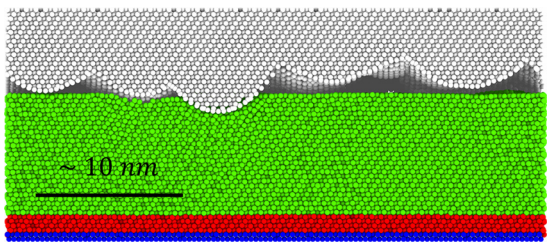	IV B 1. Multi-asperity rough contact: GW approximation
Random rough contact	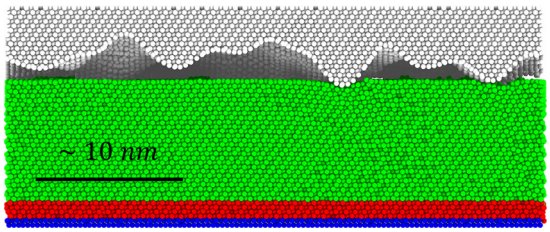	IV B 2. Randomly rough contact

adhesive contact, a modified version of Lennard-Jones (LJ) potential[34] was used

$$E(r) = 4\varepsilon((\sigma/r)^{12} - \alpha(\sigma/r)^{6}), \tag{9}$$

where r is the distance between the two atoms, ε is the depth of the potential well, and σ is the distance where the potential energy is zero. The coefficient α was introduced, as in Yang *et al.*,[21] to control the attractive long-range term. When $\alpha = 1$, Eq. (9) becomes the standard LJ potential; however, the attractive force can be removed from the formula with $\alpha = 0$. The LJ parameters for calcium reported by Shu and Davies were used: $\varepsilon = 0.21445$ eV and $\sigma = 3.5927$ Å.[35] A cutoff radius of 3σ was applied to the potential. Moreover, the potential was switched off by applying the CHARMM potential switching function[36] from a starting radius of 2.5σ. The switch ensures that there is no discontinuity jump in the force field at the cutoff radius. Although a cutoff of 3σ was introduced to the potential, the potential energy would be negligibly small at distances slightly larger than the calcium lattice parameter. Considering the potential energy of the standard LJ formula at a conventional cutoff of 2.5σ, i.e., $E(2.5\sigma) \cong 1/60\varepsilon$, the modified potential energy with $\alpha = 0$ shows almost the same value at a shorter distance of ~5.7 Å $\cong 1.6\sigma$.

C. Single asperity contact

The Hertzian contact model was simulated by bringing a deformable substrate in contact with an atomistic rigid spherical cap. In order to investigate possible size effects, different radii, ranging between 15 Å and 1000 Å, were used for generating the spherical caps. The caps were generated by bending a crystalline slab: first a crystalline slab with a thickness of three atomic layers was generated, and then the atoms were shifted accordingly to follow the geometry of a spherical cap. In this manner, an atomically smooth surface was generated that would show the most comparable stress distribution conditions with Hertz continuum mechanics.[10] Moreover, the height of the spherical caps was equal to their radii for $R \leq 100$ Å, while it was ~110 Å and 15 Å for $R =$ 200 Å and $R = 1000$ Å, respectively.

The size of the deformable substrates was different for different contact radii, in order to decrease the simulation time: each of the deformable parts contained 76 700 atoms (for radii of 15 and 20 Å), 165 056 atoms (for radii from 50 to 200 Å), and 570 960 atoms (for the 1000 Å radius), respectively. The spherical cap was moved toward the substrate with a constant velocity of 1 m/s, with a total displacement of ~14 Å.

D. Multi-asperity contact

The GW contact model was investigated by bringing a rigid rough surface comprising multiple spherical asperity tips in contact with a deformable flat counterpart, as discussed in detail in Section IV B 1. It should be noted that, assuming no asperity interactions, there is practically no difference between the case where the rough surface is

deformable and the flat one is rigid, as in the original GW model, and when the flat surface is deformable and the rough surface is rigid, as is implemented in this investigation.

First, a point cloud was created through generating a rough surface with an RMS roughness of 10 Å, a radius of 100 Å, and an asperity density of 0.001 $Å^{-2}$. The generated rough surface had 149 asperities. Then, the surface point cloud was used for constructing an atomic block. To do so, a crystalline cubic bulk with a lateral size of ~386.7 Å was generated, with [111] along its z direction. Then, the height of the surface point cloud was calibrated to have its minimum at a value of a_0. Finally, the positions of the atoms of the crystalline bulk were compared with the coordinates of the surface point cloud: the ones located above the surface point cloud were removed, and the remaining constituted a crystal structure with a rough surface of minimum thickness of a_0. It should be noted that the surface point cloud itself was also added as an extra atomic layer to the top of the constructed substrate, in order to keep the substrate's surface the same as the generated one, with no stepped structure.[37]

The counterpart was generated with the same lateral length, but with an atomically flat surface, and a thickness of 18.5 a_0, built from 364 861 atoms. Because this flat counterpart was meant to be deformable, it was divided into three layers as described in Section III A.

E. Randomly rough contact

A randomly rough contact was simulated for comparison with the multi-asperity contact and, later, with Persson's model. In order to generate a comparable randomly rough surface, first, the lateral correlation length L_c of the GW surface was calculated. Then, using the values of L_c and the RMS roughness of 10 Å, a Gaussian randomly rough surface was generated following the method outlined by Bergström *et al.*[38] The surface point cloud was used for building a system with the same features as those described for the multi-asperity contact. Additional details are given in Section IV B 2.

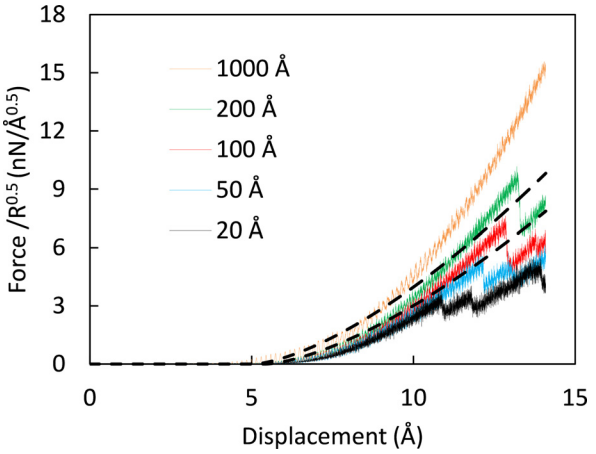

FIG. 2. The variation on the normal forces, normalized by the indenters' radii, as a function of displacement. The reference point of the displacement axis is the initial position of the indenter. The dashed lines show the best fits to the curves of $R = 100$ Å and $R = 200$ Å, based on Hertzian theory. The sudden drops are indications of dislocation sliding in the systems, i.e., the initiation of plastic deformation.[37]

IV. RESULTS AND DISCUSSION

The results of the single asperity, multi-asperity, and randomly rough contacts are discussed in Sections IV A and IV B with reference to potential size effects.

A. Single asperity contact size effects

The force-displacement curves of a number of contacts with spherical cap indenters of various sizes are shown in Figure 2. The indenters were moved by controlling their displacement. The results show that larger indenters applied larger forces for the same displacement values. Moreover, a number of load drops are noticeable for all but the largest indenter. In the nanoindentation process, the first load drop indicates the onset of plastic deformation, which is a result of the nucleation of dislocations, and their movement and interactions; readers are referred to the literature[37,39,40] for detailed analyses on dislocation behaviors during the nanoindentation process. As is shown in Figure 2, the plastic deformation was initiated at a larger penetration depth as a bigger

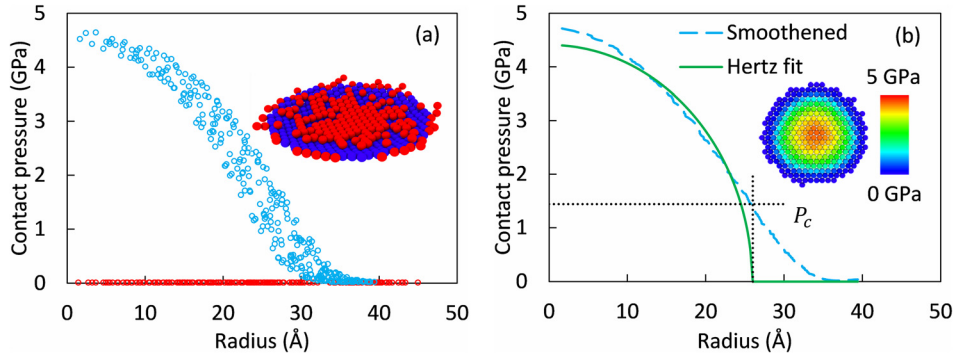

FIG. 3. The interfacial distribution at the contact as a function of radial distance from the center of the contact was obtained from the atoms of the spherical caps. This figure corresponds to $R = 100$ Å, at a strain prior to the onset of plastic deformation. (a) The atoms of the cap with a non-zero interfacial stress were selected; the red colored data points were identified as false positives and were removed by applying an empirical interacting pressure threshold value of $P_i = 0.02$ GPa. (b) The Hertz theory was fitted to the smoothened interfacial pressure distribution. The interacting atoms are also shown, colored corresponding to their interfacial pressure values. The fitted contact radius was used to define a contact pressure, as illustrated; this P_c was later used to define the contact distance, as discussed in Section IV A 2.

indenter was used for the simulation. When fitting the Hertz theory to the elastic part of the force-displacement curves, the reduced Young's moduli were found to be $E^*_{R=100\text{Å}} = 23.18\,\text{GPa}$ and $E^*_{R=200\text{Å}} = 27.17\,\text{GPa}$; however, the fitted constant values could not correctly describe the systems' mechanical behavior for the complete range of elastic deformation. The same trend of these results, i.e., the increase in E^* for larger indenters, and the inability of describing the contact behavior for the whole range of elastic deformation, can be found in the literature.[40] Therefore, instead of the conventional method of fitting the Hertz theory to the force-displacement curve, the mechanical behavior of the contacts was investigated through their pressure distributions and their comparison with the Hertzian solution (see Section II A). It should be noted that the fitting process was done for the range up to and excluding the initiation of plastic deformation. Moreover, these simulations were used to define a contact distance for non-adhesive contacts.

1. The fitting procedure

In order to compare the results with Hertzian mechanics, two conditions were considered for extracting data from the simulations: first, the deformation should be in the elastic regime, i.e., before the onset of plastic deformation, and, also, the stress field initiated at the contact should not extend beyond the substrate so that it could be fully enveloped within the simulation box (see Appendix B).

The Hertz formula for the contact pressure needed to be fitted to the values extracted from the simulations. To do so, the interfacial stress values of the indenters' atoms were calculated, and the values were saved with 2 decimal place precision. Then, all atoms that had non–zero interfacial stress were selected (see Figure 3(a)). The distribution of the interfacial stresses showed two different patterns: one comparable with the Hertz theory, albeit with a "pressure tail,"[21] and one with very low stresses distributed sparsely over the contact area. The pressure tail of the first pattern and the second pattern itself, both, have the same justification: the weak interfacial stress values are detectable in the atomistic model due to the applied long-range interaction between the contacting

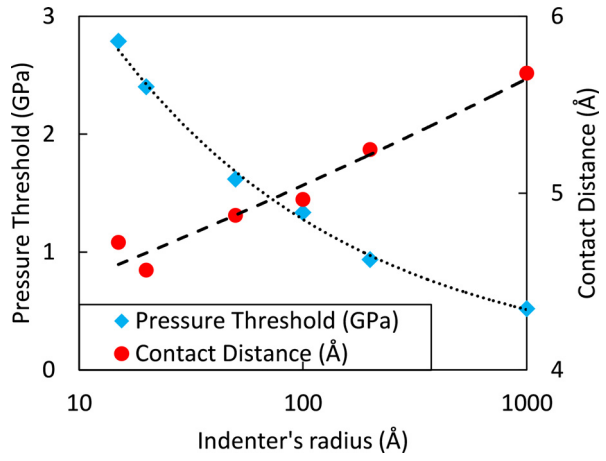

FIG. 4. The dependence of the pressure threshold and the contact distance on the indenter's radius. The dotted curve and dashed line illustrate the trends.

atoms, which is not considered in non-adhesive contact mechanics theories. The pressure tail results from the atoms that are radially far from the center of the contact. On the other hand, the second pattern is mostly a consequence of the weak interactions of the atoms that are radially close to, but vertically far from the center of the contact: these are the atoms of the second atomic layer of the spherical caps. In order to remove the atoms occurring with the second pattern, and which can be considered as false positives, an empirical interacting pressure threshold value of $P_i = 0.02\,\text{GPa}$ was determined by examining all of the studied systems and identifying the pressure values associated with false positives. This threshold removed false positives and had a negligible effect on the pressure tail (see Figure 3(a)). After filtering the data using the proposed threshold, the data were smoothened using a moving average filter with a span of 1% of the data points. Finally, the fitting procedure was performed for pressures equal to or greater than the mean pressure of each system. These steps are illustrated in Figure 3.

2. The contact distance

The Hertz theory was used to define a contact distance by applying a contact pressure P_c: the atoms with interfacial stresses lower than P_c were assigned to be out of contact. This contact pressure was defined by comparing the smoothened pressure distribution of a given simulated system with its corresponding fit, prior to the onset of plastic deformation. The pressure at the fitted contact radius was selected as P_c, and the contacting atoms were identified by filtering using the corresponding P_c. These atoms were used for defining the contact distance in a two-step procedure. First, the distances between the contacting atoms and the atoms of the substrate were calculated, and, for each atom, the minimum of the distances was selected as its contact distance. Then, the maximum of the contact distances was defined as the contact distance of the system, d_c.

The obtained values of P_c and d_c are summarized in Figure 4. As the results show, the values of these two parameters vary with the indenter size: the smaller the radius of curvature, the larger the value of P_c, while an inverse behavior can be noticed for the values of d_c. The same behavior has been reported by Yang *et al.*[21] for a system simulated by a multiscale molecular dynamics approach.

By fitting a power law to the obtained contact distances, one can estimate the values of d_c from

$$d_c \cong 4R^{0.05}. \tag{10}$$

3. The mechanical behavior

For the simulated material, the values of E and ν are reported to be 26 GPa and 0.3, respectively.[32] Therefore, the reduced Young's modulus was calculated to be $E^* = E/(1-\nu^2) = 28.57\,\text{GPa}$. In order to compare the results with the Hertz theory, the value of the variable E^* was estimated based on the pressure distributions at the contacts.

Through the fitting procedure, the contact area and the maximum pressure values were estimated for the Hertz

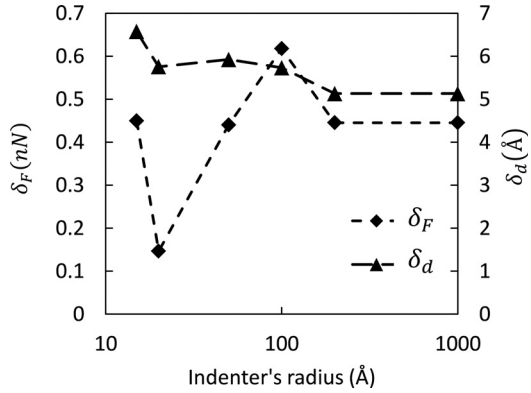

FIG. 5. The corrective displacement shifts (δ_d, δ_F) as functions of indenter radius, which were used for the conversion of the force-displacement curves into force–indentation depth ones.

contact. Using the formulas for r_c (Eq. (1)) and p_0 (Eq. (2)), one can conclude that

$$E^* = \frac{\pi}{2} p_0 \frac{R}{r_c}. \tag{11}$$

The values of E^* for each system were estimated at different values of indenters' displacement. In order to convert the indenters' displacement into the indentation depth, the following procedure was followed for all systems. Each system was analyzed at various time steps t, and, using the fitted values of p_0 and r_c at each time step, the values of the reduced modulus E_t^* (using Eq. (11)), the force $F_t = 4/3E_t^* R^{-1} r_c^3$ and the interference $d_t = r_c^2/R$ were calculated, where the subscript t specifies the corresponding time step. Then, the absolute error between the fitted values of force and the simulation results was calculated via $\varepsilon = |1 - F_{t,fit}/F_{t,simulation}|$. The time step at which the absolute error value reached its minimum was selected as the reference point for the conversion of displacement into indentation depth: it was assumed that the actual indentation depth was the value of $d_{t,fit}$ at the reference point. Hence, a shift was defined as $\delta_d = d_{t,simulation} - d_{t,fit}$, and all displacement values were shifted using δ_d. In order to make sure that the force was zero at zero indentation depth, a force shift was similarly defined as $\delta_F = F(id = 0)$, where id is the newly estimated indentation depth. Therefore, the origins of the force-displacement curves were shifted by the corresponding values of (δ_d, δ_F) in order to estimate the force-indentation depth curves. These corrective displacement shifts are summarized in Figure 5.

Figure 6(a) shows the fitted Young's moduli: the fitted E^* values reveal that this parameter is highly strain-dependent at the very early stages of contact, in contrast to the conventional definition of E^* as a constant value. The results show that the contact behaved as "softer" at shallow indentation depths, and the contact's elastic modulus increased toward the bulk value of 28.57 GPa as the contact approached the point of initiation of plastic deformation. Moreover, it can be seen that the radii of curvature at the contact influenced the fitted E^* values; a normalized representation would give a better insight into this effect. Figure 6(b) shows the fitted E^* values as functions of the normalized indentation depth (d) by the corresponding tip's radius (R), i.e., d/R. Figure 6(a) reveals that the two smallest contact radii, namely, 15 Å and 20 Å, behaved differently from the other systems.

In order to explore these behaviors further, the number of interacting atoms (N_i), detected based on the pressure threshold of 0.02 GPa (see Figure 3), was investigated. Figure 7 shows the values of N_i, normalized with the contacts' radii, as a function of indentation depth. This figure shows that the number of the interacting atoms was increasing as the indentation depth was increased. For the smallest contact radius, i.e., $R = 15$ Å, these increments occurred in large steps. These steps became smaller as the indenters were enlarged, resulting in a linear behavior for $R \geq 50$ Å. On the other hand, some fluctuations are visible for the largest system, i.e., $R = 1000$ Å, as is also reflected in Figure 6(a). It should be noted that this behavior could also have occurred due to the system's size and the sampling time: as the systems became larger, their stability was increased, while the sampling time remained the same. Consequently, the extracted data for the smaller systems were essentially an average of all the fluctuating values, while for the largest one, the extracted data needed to be smoothened to filter out the fluctuations. At the same time, it should be noted that a smaller sampling time would potentially reveal fluctuations in the other systems as well.

Although Figure 6(b) shows that the values of the fitted E^* are not exactly a linear function of d/R, assuming a linear relation for shallow indentations helps us to predict the values of E^*. The slope of the fitted E^* values versus d/R, as shown in Figure 6(b), was calculated for the ranges of data with the fitted $E^* \leq 25$ GPa of each system, which corresponds to the indentation depth of ~4 Å, as shown in Figure 8. This behavior describes E^* as a function of indentation depth and the indenter's radius in the form of

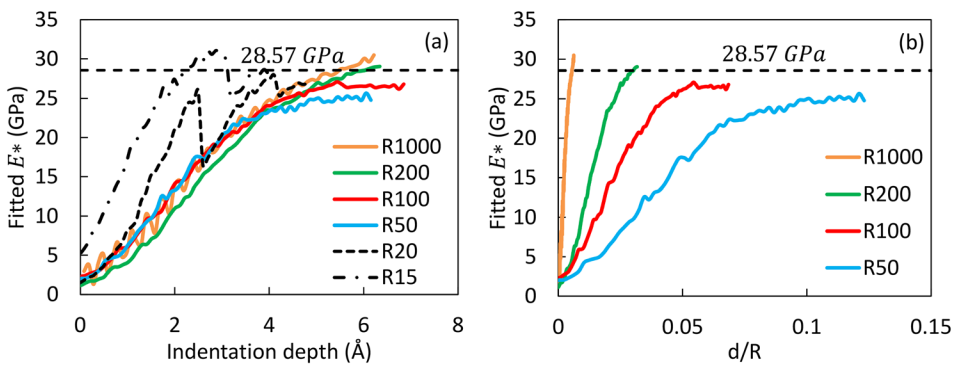

FIG. 6. Variation of the fitted values of E^* as a function of (a) the indentation depth and (b) the normalized indentation depth by the corresponding values of the tip's radius. Note that i in Ri indicates the size of contact radius, e.g., R50 ≡ ($R = 50$ Å).

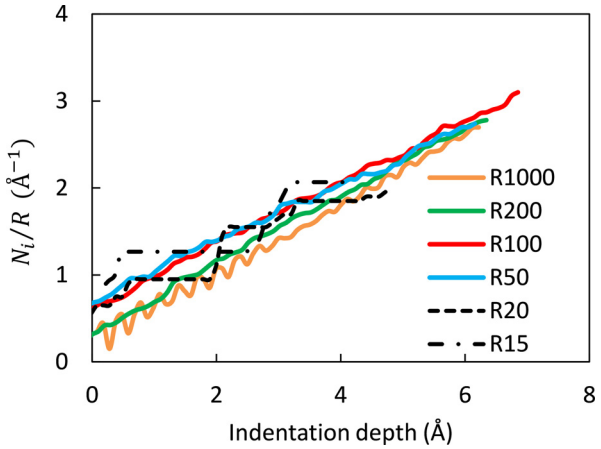

FIG. 7. The number of interacting atoms (N_i), based on the pressure threshold of 0.02 GPa, normalized by the contact's radius, i.e., N_i/R, increases with increasing indentation depth.

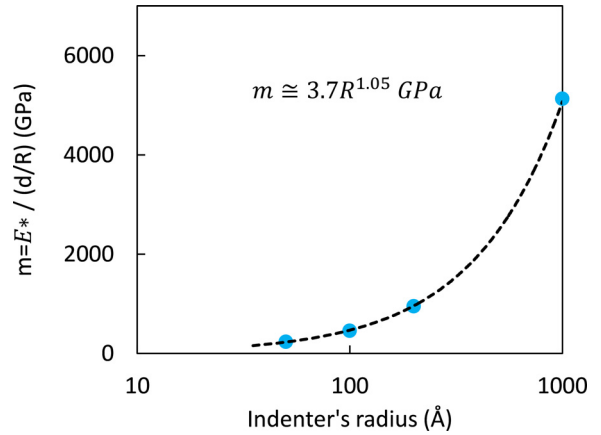

FIG. 8. The rate of change of the fitted E^* values as a function of the tip's radius.

$$E_c^* = C + md/R, \tag{12}$$

where C is a constant found to be ~2.1 GPa, and m is a power law function in the form of $m = AR^B$; for the current system, it was found that $m \cong 3.7R^{1.05}$ GPa. This empirical formula describes the parameter E^* as a function of the contact geometry, i.e., the indenter's size and the indentation depth, as well as the mechanical properties of the contacting materials. The value of E_c^* increases and tends to the bulk value by increasing the indentation depth up to a finite value, which is ~4 Å in the current study; however, the way E_c^* varies as a function of the indenter's size depends on the value of the exponent B. While the contact geometry appears directly in the formula for E_c^*, the mechanical properties of the contacting materials are embedded in the values of constants A, B, and C. The nonzero value of C, which suggests a finite value of E^* at the limiting case of zero indentation depth, is a consequence of defining an interacting pressure threshold $P_i = 0.02$ GPa for identifying the interacting atoms and fitting the Hertz formula to the pressure distribution of those atoms. In order to show this effect, let us assume a limiting case of two interacting atoms: for this conceptual system, the Young's modulus can be defined as $E = \sigma_{eng}/\varepsilon_{eng}$, where σ_{eng} and ε_{eng} are the engineering stress and engineering strain, respectively, which can be rewritten as $\sigma_{eng} = F_\perp/A_a$ and $\varepsilon_{eng} = \delta_r/r_i$, where r_i is the interacting distance between the two atoms and δ_r is an infinitesimal change in r_i. The Young's modulus can be rewritten as $E = \frac{F_\perp/A_a}{\delta_r/r_i} \sim \frac{r_i}{A_a} \cdot \frac{dF_\perp}{dr} = 168\varepsilon\sigma^6 r_i^{-7} A_a^{-1}$; therefore, the Young's modulus would have a nonzero value at any interacting distance r_i. In the current study, the interacting distance was defined by an interacting pressure threshold, and by replacing σ_{eng} with P_i, a corresponding contact force can be estimated as $F_i = P_i A_a$. Then, the interacting force can be calculated as $F(r) = 48\varepsilon\sigma^{12}/r^{13}$, which results in $r_i = 6.417$ Å, for $F(r) = F_i$. (See Section IV A 4 for the calculation of A_a.) Therefore, the corresponding value of the Young's modulus can be estimated to be $E \cong 2.27$ GPa. Although this crude estimation of the Young's modulus, which is close to the value of $E_c^*(d = 0) = C = 2.1$ GPa, cannot be directly translated into the contact's elastic modulus, it appears to justify the nonzero value of the constant C.

The Hertz formula was solved using the fitted values of E^*, the bulk value of $E^* = 28.57$ GPa, and the estimated values from Eq. (12), as shown in Figure 9. As the results show, the fitted values of E^* describe best the systems' behavior through the whole indentation process, as was expected, while the values estimated with Eq. (12) are valid only for very shallow indentation depths. On the other hand, the bulk value of $E^* = 28.57$ GPa appears to fit better to the results for indentation depths larger than ~4 Å. Therefore, as the results show, assuming the applicability of the Hertz theory at the atomic scale, a redefined value of E^* is needed to describe contacts at shallow indentation depths.

4. The contact area

In this section, the correctness of the proposed pressure cutoffs was investigated by comparing the Hertz solution with the estimated contact areas based on the contact distances. Hertzian mechanics suggest a relation between the radius of the contact area r_c, the indenter's radius, and the indentation depth in the form of $d = r_c^2/R$. The radii of the contact areas for each of the simulated systems were estimated as follows: first, the contacting atoms were identified. Then, the real contact area was estimated via $A_{real} = N_c A_a$, where N_c is the number of the contacting atoms and A_a is the projected area of an individual atom, estimated from $A_a = \pi/4 d_a^2$, where d_a is the atomic diameter, which is 3.94 Å for the current study (see Appendix A). Finally, assuming the contact area to be a circle, the radius of the contact was calculated. Figure 10 shows the radii of contact normalized by the indenters' radii versus the indentation depth.

The results show that the estimated contact areas based on the contact distances were in good agreement with the Hertz solution, which verifies the proposed contact distance definitions, as well as the method used for the conversion of the indenters' displacement into indentation depth.

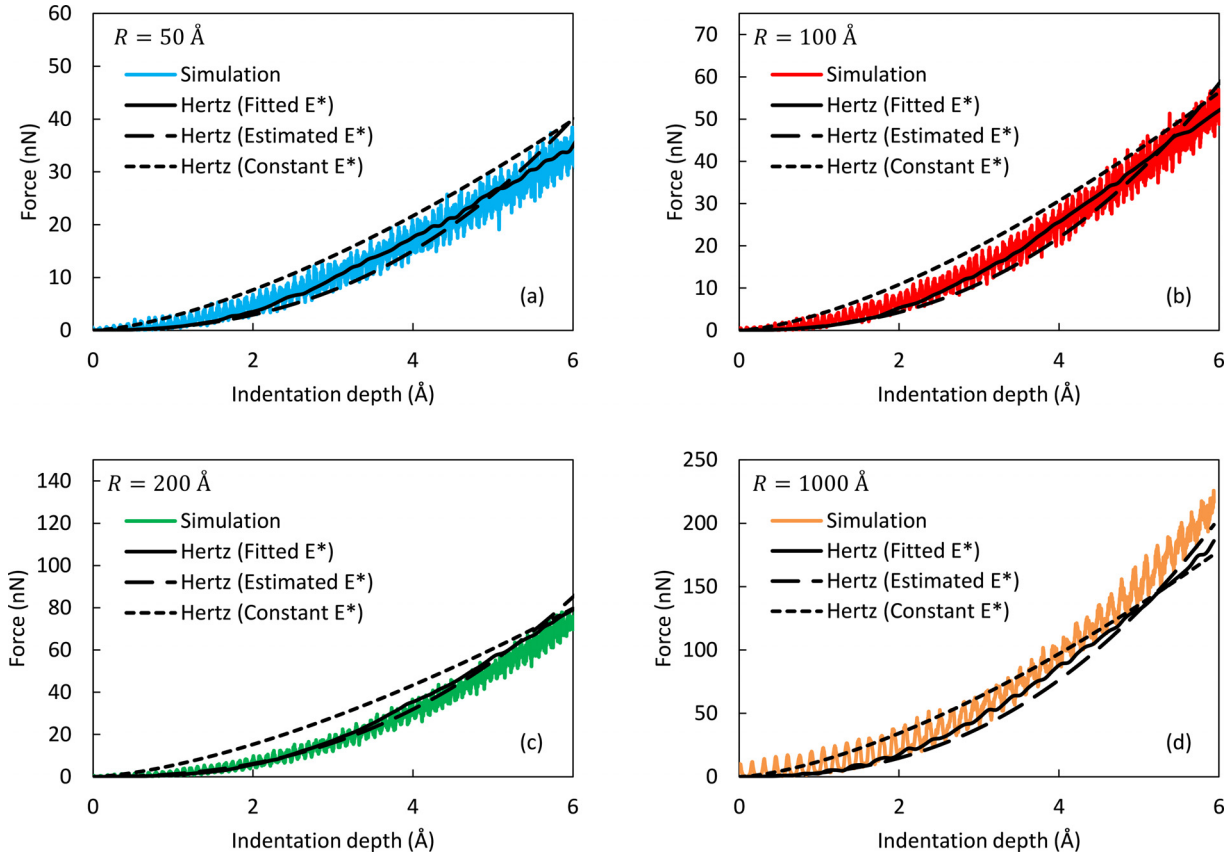

FIG. 9. The force–indentation depth curves from simulations were compared to the Hertz theory using the fitted values of E^* based on Eq. (11), the estimated ones from Eq. (12), and the constant bulk value of $E^* = 28.57$ GPa for the spherical caps with (a) $R = 50$ Å, (b) $R = 100$ Å, (c) $R = 200$ Å, and (d) $R = 1000$ Å. Note that the axes ranges are different.

5. Contacting atoms versus interacting atoms

The agreement between the estimated contact area and the Hertz solution implies that there is a distinction between the interacting area and the contacting area, where the former can be calculated from the interfacial pressures and the latter can be estimated based on the defined contact distances; however, one may wonder if these two areas result in the same contact behavior. This issue can be investigated by comparing the number of interacting atoms (N_i) and the number of contacting atoms (N_c). Figure 11 shows that the ratio of N_c/N_i is very small at the beginning of the contact; however, with increasing indentation depth, N_c and N_i changed with different rates in a way that the ratio of N_c/N_i tended to 1.

Aside from the essentially different behavior of the contact with $R = 15$ Å, the results show a clear size effect: *the*

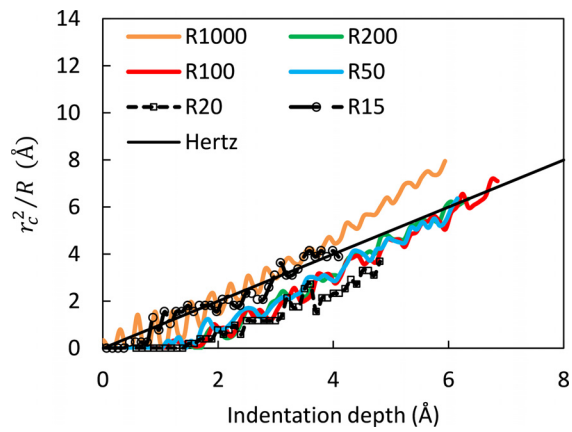

FIG. 10. The normalized contact area as a function of indentation depth.

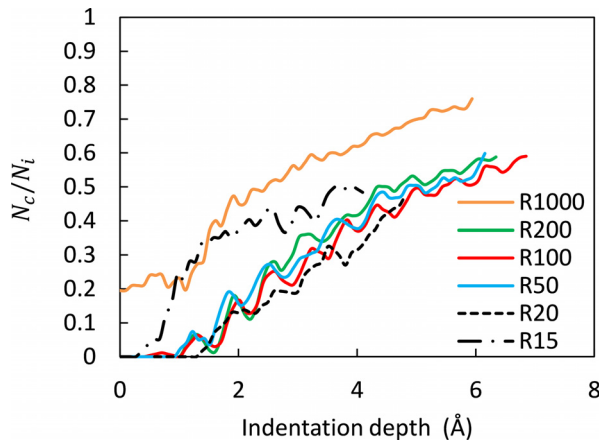

FIG. 11. The number of interacting atoms (N_i) and the number of contacting atoms (N_c) change with different rates as the indentation depth increases. It should be noted that the results were smoothened with a moving average filter with a span of 5% of the data points, in order to remove the fluctuations due to the sampling sizes, as is discussed in Sec. IV A 3.

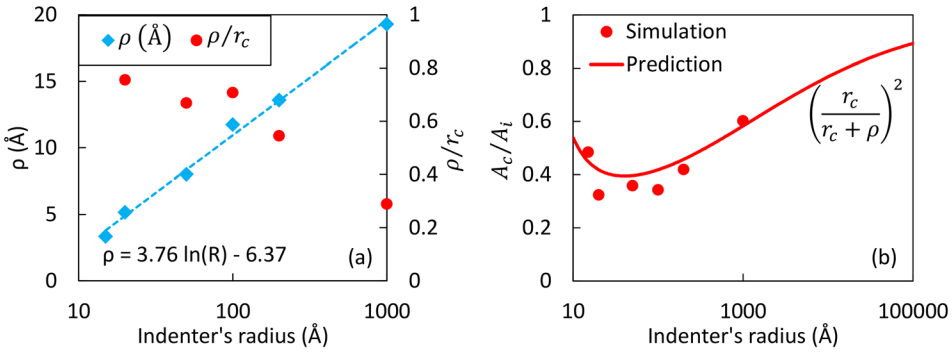

FIG. 12. (a) The length of the pressure tail, ρ, was calculated at a displacement of ~ 4 Å, and described by a natural logarithmic function of the indenter's radius. Moreover, the figure shows that the ratio ρ/r_c decreases with increasing indenter size. (b) The ratio of A_c/A_i of, both, the simulation results and the prediction method is shown. The prediction is based on the Hertz contact theory, i.e., $r_c = \sqrt{Rd}$, and the values of ρ calculated in (a).

TABLE II. The steps of the methods used for estimating the values of the relative projected contact area.

Projection method	1- Identification of the contacting atoms through the definition of contact distance
	2- Visualization of the contacting atoms
	3- Analysis of the projection of the contacting atoms on a lateral (xy) plane
GW	1- Detection of the local maxima and construction of PDF of the identified asperities
	2- Solving Eqs. (4) and (5)
Persson (Eq. (7))	1- Calculation of the PSD of the rough surface
	2- Integration of PSD in the form of Eq. (7)
	3- Solving Eq. (6)
Persson (Eq. (8))	1- Calculation of the probability distribution of the interfacial pressure values
	2- Fitting of the double Gaussian function in the form of Eq. (8) to the interfacial pressure distribution of the system
	3- Solving Eq. (6)

contact area tends to the interacting area with increasing indenter size. This effect can be related to the atoms responsible for the tail appearing in the pressure distribution, as described in Section IV A 1: practically, the contact area tends to the interacting area with increasing indenter size as the pressure tail length becomes negligibly small and the pressure distribution increasingly approximates the Hertzian one. More specifically, as the interacting area increases, the contact area increases faster than does the length of the pressure tail. In order to demonstrate this, the systems were analyzed at a displacement of ~ 4 Å: the lengths of the pressure tails were estimated via an empirical formula as a function of the indenter radius, as is shown in Figure 12(a), which shows that the ratio ρ/r_c decreases as the indenter's size increases. Furthermore, the ratio A_c/A_i can be predicted by $(r_c/(r_c+\rho))^2$, where $r_c = \sqrt{Rd}$, with $d = 4$ Å, and $\rho = \rho_1 \ln(R) + \rho_2$ is the length of the pressure tail, and ρ_1 and ρ_2 are the fitted constants. Figure 12(b) shows the comparison between the predicted ratios of A_c/A_i and the simulation results.

B. Rough surface contacts

In order to estimate the projected contact area of the rough surface contacts, different approaches were applied, which are summarized in Table II. In the "projection method," the mean value of the radius of curvature R for the rough surface was estimated; the mean value of the radius of curvature for the constructed surface was estimated through its definition of $\boldsymbol{R} = |(1+\mathbf{z}'^2)^{3/2}/\mathbf{z}''|$, where $\mathbf{z}'$ and $\mathbf{z}''$ are the first and second derivatives of the surface heights, respectively; then, R was defined as $\sqrt{R_x \cdot R_y}$. Using the calculated R and Eq. (10), a contact distance was defined in order to identify the contacting atoms. Then, the projected area of the contacting atoms on a plane normal to the applied force, i.e., the xy plane in the current study, was estimated as the projected contact area A_{pc}. The relative contact area was easily

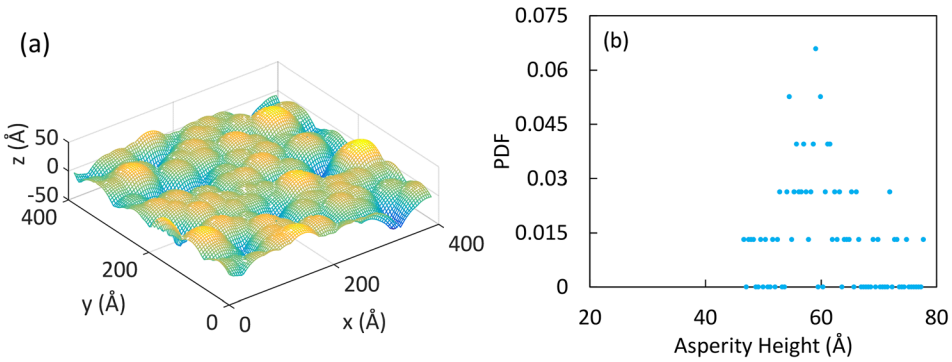

FIG. 13. (a) The generated GW surface with $\sigma = 10$ Å, $R = 100$ Å, and $\eta \cong 5 \times 10^{-4}$ Å^{-2}, and (b) its PDF of asperity heights with 76 detected asperities.

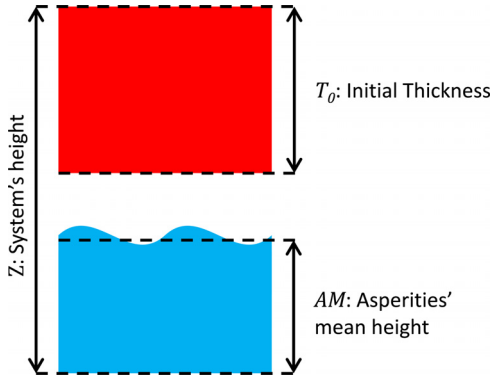

FIG. 14. The schematic of the GW contact simulations. The separation was defined as $s = Z - (AM + T_0)$.

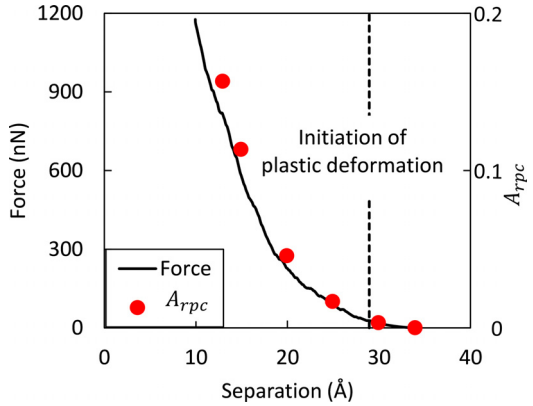

FIG. 15. The simulation results of the GW contact. The continuous line shows the external contact force, while the dots show the value of A_{rpc} at different values of separation.

calculated from the ratio $A_{rpc} = A_{pc}/A_0$. In another approach, the GW model was used for estimating the contact behavior of the rough contacts. To do so, Eqs. (4) and (5) were solved, and the results were normalized with the nominal contact area A_0, in order to achieve the relative projection contact area A_{rpc} and the nominal pressure, respectively. The value of R was estimated as mentioned above. Moreover, the local maxima were detected and identified as asperities; therefore, the probability distribution function (PDF) of the asperities could be generated, which was needed for solving the GW model. Finally, for the randomly rough surface, the Persson model, i.e., Eq. (6), was used. The value of the parameter G was found from, both, Eqs. (7) and (8). It should be noted that in order to work with Eq. (7), the PSD of the rough surface was needed, which was estimated via with the algorithm described by Persson *et al.*[41]

The contact behavior of the systems was analyzed using the methods that are summarized in Table II, and the results are presented and discussed in Sections IV B 1 and IV B 2. It should be noted that the system was analyzed up to the point that the stress field reached the rigid layer and not beyond that (see Appendix B).

1. Multi-asperity rough contact: GW approximation

The generated multi-asperity rough surface with the estimated probability distribution function (PDF) is shown in Figure 13.

The mean value of the radius of curvature for the constructed surface was estimated to be ∼111 Å, which is slightly larger than the assigned value of 100 Å for the generation of the surface. It should be noted that the estimated value of $R = 111$ Å was used for working with the GW model.

In order to analyze the results, first, the mean plane separation was estimated using the height of the simulation box, the initial thickness of the deformable body, and the asperity mean height of the rough substrate, as demonstrated in Figure 14. The atomistic system was analyzed by identifying the contacting atoms by applying a contact distance of $d_c = 5.062$ Å. Using the projection method (see Table II), the projected area of the contacting atoms was estimated as the projected contact area A_{pc}. Table III shows the projection of the contacting atoms under increasing contact force. The relative projected contact area ratio A_{rpc} and the mechanical response of the contact are shown in Figure 15.

In order to estimate the contact force using the GW model, the reduced Young's modulus of $E^* = 28.57$ GPa was used; the reason was the initiation of local plastic deformations, suggesting that the indentation depth for each individual spherical contact was large enough for the bulk value of E^* to have been reached. The results are shown in Figure 16.

2. Randomly rough contact

The GW surface was analyzed, and its lateral correlation length was found to be ∼23.4 Å. Using this value and $\sigma = 10$ Å, a comparable randomly rough surface with a normal distribution of heights was generated, as shown in Figure 17.

The projected contact area at different pressure values was estimated via all four mentioned approaches in Table II. In order to estimate the contact area via the projection

TABLE III. The black dots are the projection of the contacted atoms of the GW surface. The first row indicates the contact force in units of *nN*.

1.49×10^{-5}	18.15	91.15	228.18	582.30	814.50
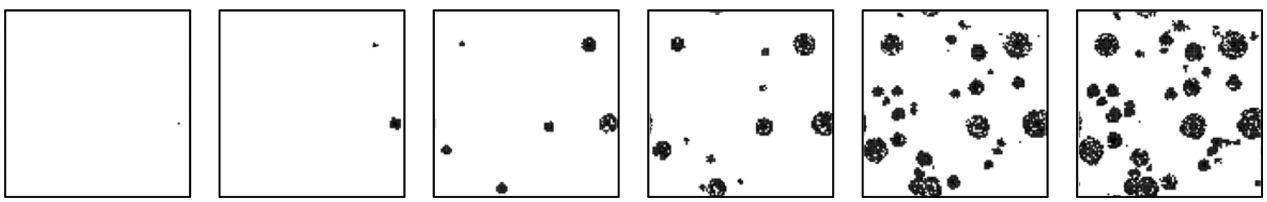					

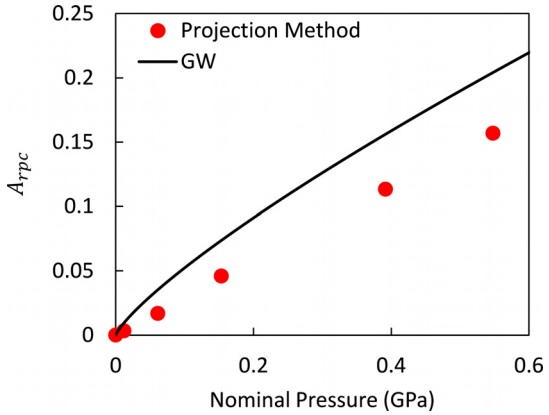

FIG. 16. The relative projected contact area as a function of nominal pressure for the GW type multi-asperity rough surface.

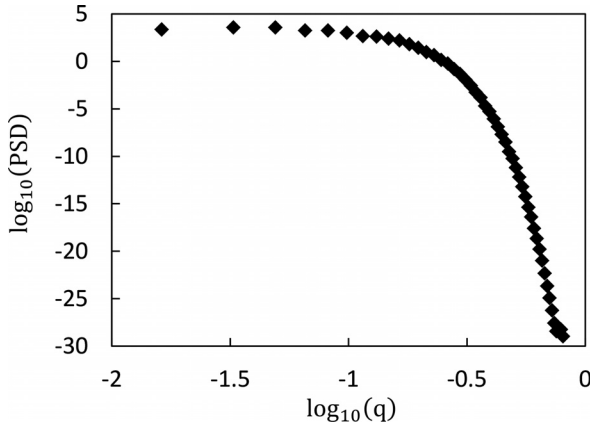

FIG. 18. The calculated PSD of the randomly rough surface.

method, the mean radius of curvature of the rough surface needed to be calculated. This value was found to be 112 Å, which was almost equal to $R \cong 111$ Å of the simulated multi-asperity surface. Using Eq. (10), a contact distance of 5.064 Å was defined for identifying the contacting atoms. Table IV shows the projection of the contacted atoms at different separations.

The GW model was applied to the surface in the same way that was done for the GW-type rough surface (see Section IV B 1). In order to estimate the contact behavior using the Persson theory, first, the value of G was calculated based on Eq. (7). The needed PSD for estimating the parameter G from Eq. (7) was calculated following the algorithm described by Persson *et al.*[41] (see Figure 18), and the value of G was calculated to be 2.57 GPa^2, with $E^* = 28.57$ GPa, and $\zeta q_L = q_H$ at a length scale of $\lambda \cong 7.8$ Å.

Furthermore, the Persson model was used with the value of $\bar{G}$ as the fitting parameter of Eq. (8). To do so, the interfacial pressure distributions were calculated at different nominal pressure values from the simulation results. Then, the pressure distributions were smoothened using a moving average filter with a span of 1% of the data points. Finally, Eq. (8) was fitted to the pressure distribution, and $\bar{G}$ was found. Figure 19 shows the interfacial pressure distribution of the contact at a nominal pressure of $P_0 = 0.39$ GPa. It should be noted that the difference between the simulation results and Eq. (8) for small pressure values is due to the long-range interactions that may not be negligible in the atomistic simulations, but are absent in non-adhesive contact theories.[21]

Figure 20 compares the contact behavior of the randomly rough surface, estimated using all approaches of Table II. As the results show, for light squeezing pressures, the estimations of, both, the Greenwood-Williamson and Persson theories overestimate the results from the projection of the contacting atoms. Moreover, it can be noticed that if the parameter G is found using Eq. (8), the Persson model overestimates the contact area at very small pressures, and then tends toward the

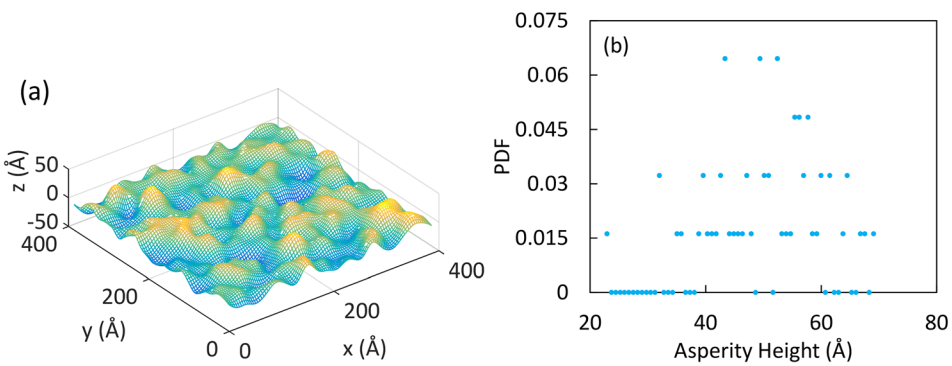

FIG. 17. (a) The generated randomly rough surface with a correlation length of 23.4 Å, and $\sigma = 10$ Å, and (b) its PDF of asperity heights with 62 detected asperities.

TABLE IV. The black dots are the projection of the contacted atoms of the randomly rough surface. The first row indicates the contact force in units of *nN*.

4.64×10^{-4}	12.18	53.36	165.33	446.96	575.32
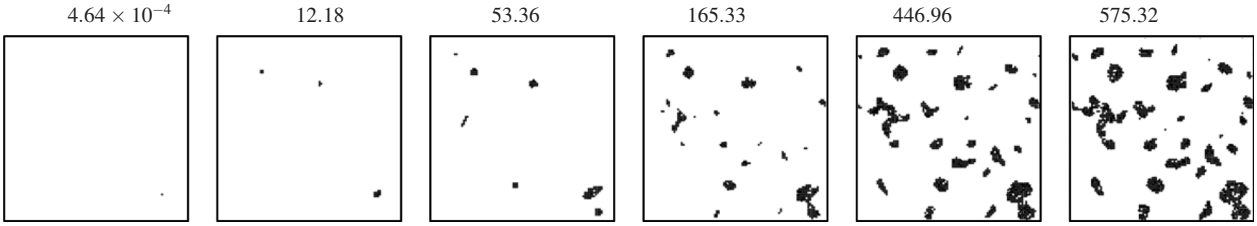					

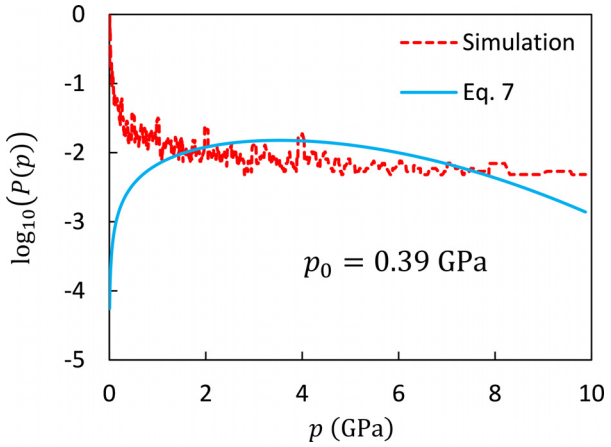

FIG. 19. The interfacial pressure distribution $P(p)$ at the nominal pressure of $p_0 = 0.39$ GPa.

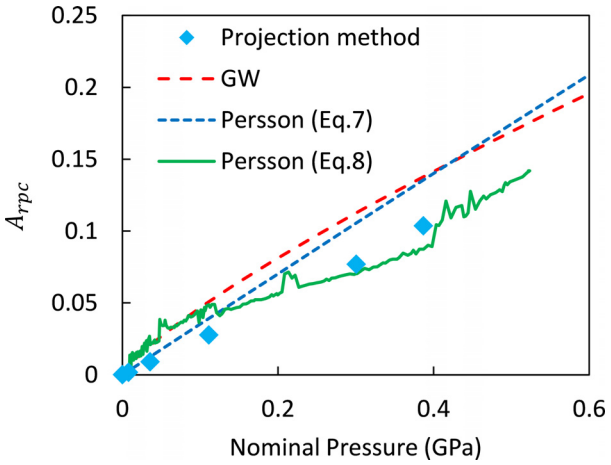

FIG. 20. The relative projected contact area as a function of nominal pressure for the randomly rough surface.

results of the projection method. The reason is that the pressure distribution contains all the interacting atoms, and not only the contacting ones, which affects the fitted values of $\bar{G}$; however, with increasing indentation depth, the number of contacting atoms tends toward the number of the interacting ones, as was discussed in Section IV A 5. Therefore, as the nominal pressure increases, the contribution of the contacting atoms will be larger in the pressure distribution, which will be directly reflected in the fitted values of $\bar{G}$, and consequently, the description of the Persson model would be closer to the results of the projection method.

a. Effects of the length scale on the estimation of the contact behavior. The value of G can be defined as $G = \frac{1}{8}E^{*2}\langle|\nabla h|^2\rangle$ (see Section II C). Assuming $r = G/\bar{G} = 1$, with $\bar{G}$ being the fitting parameter of Eq. (8), the values of the contact modulus can be estimated via $E^* = \sqrt{8\bar{G}/\langle|\nabla h|^2\rangle}$; therefore, the length scale that is used in the calculation of the mean square gradient of the rough surface can affect the estimated value of E^*. Figure 21(a) shows the values of $\langle|\nabla h|^2\rangle$ calculated at different length scales, while the corresponding fitted values of E^* at two different length scales are shown in Figure 21(b).

Considering the calculation method of $\bar{G}$, which is performed at the lowest length scale of the system, a reasonable length scale for the calculation of the mean square gradient would be $\lambda = 2\delta$; however, this would result in low values of E^*, as is shown in Figure 21(b).

The values of G can be calculated at different length scales by assuming that the reduced modulus is $E^* = 28.57$ GPa. It was found that $G(\lambda = 2^6\delta) = 2.60\,\text{GPa}^2$ had the closest correspondence to $G = 2.57\,\text{GPa}^2$, which was calculated based on the PSD of the surface with $q_H = 2\pi/2\delta$. This inconsistency between the length scales could be a consequence of converting the definition of G from the original form of Eq. (7) into $G = \frac{1}{8}E^{*2}\langle|\nabla h|^2\rangle$ using the second moment of the PSD, as described in Section II C. Considering the results that are presented in Figure 20, calculating the theoretical value of G in the form of Eq. (7) appears to resolve this issue.

3. Comparison between studied rough surfaces and their contacts

In order to compare the surfaces, a number of statistical data were calculated for both surfaces, and the results are summarized in Table V. Note that all calculations were performed at the lowest length scale of $\lambda = 2\delta \cong 7.8$ Å.

For light squeezing pressures, the rough surface analytical models predict that the contact area increases linearly with the nominal pressure in the form of $A_{rpc}=\kappa(P_0/(E^*\sqrt{\langle|\nabla h|^2\rangle}))$.[42] In order to compare the contact behavior of the rough surfaces, the nominal pressure values were normalized by E^* =28.57 GPa and the corresponding values of root mean square gradient. Figure 22 shows the results of this comparison: the contact behavior of both systems was very close. Such behavior was also reported for a contacting system composed of nickel atoms.[4] Moreover, for the simulated

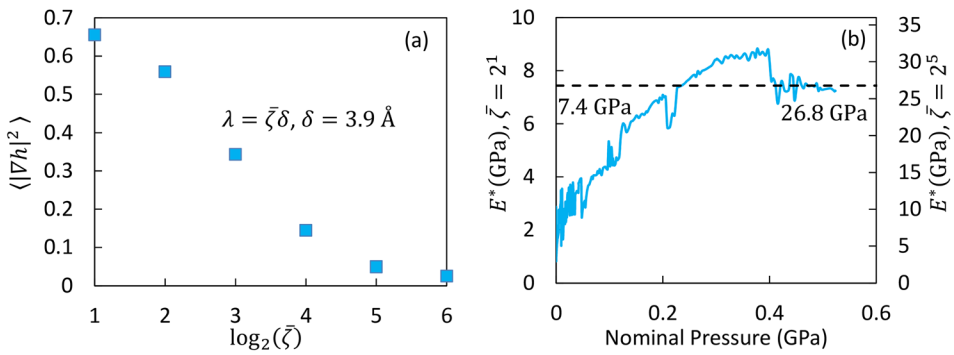

FIG. 21. (a) The effect of the length scale on the mean square gradient of the rough surface. The length scale is defined as $\lambda = \bar{\zeta}\delta$, where $\delta = 3.9$ Å is the lateral distance between two neighboring atoms of the rough surface. Note that $\bar{\zeta} \neq \zeta$. (b) The dependence of the fitted values of E^* to the nominal pressures using two different length scales (on the left and right vertical axes).

TABLE V. The statistical calculated values for the studied rough surfaces.

	σ (Å)	$\langle\|\nabla h\|^2\rangle$	Skewness	Kurtosis
GW type	9.82	0.58	−0.64	4.05
Randomly Rough	9.67	0.65	−0.05	3.05

systems, the proportionality coefficient was calculated to be ∼6.2, which is larger than the corresponding value of, both, the elaborated multi-asperity models, i.e., $\sqrt{2\pi}$, and the Persson theory, i.e., $\sqrt{8/\pi}$.[42] This could be a result of the lateral resolution for the calculation of the mean square gradient of the rough surfaces, as is demonstrated and discussed in Section IV B 2 a.

V. SUMMARY AND CONCLUSIONS

In this paper, a number of continuum models for non–adhesive contacts were investigated at the atomic scale and it was revealed that the atomistic behavior is rather different from the continuum descriptions, especially at the very first stages of the contact.

First, the Hertz contact model predictions were compared to the simulated force-displacement curves; however, large discrepancies between the two were found. Therefore, the pressure distributions were analyzed instead, in order to calculate the reduced Young's moduli. It was found that the values of E^* were increasing in the form of $E^*_{c_o} = C + AR^{B-1}d$ for shallow indentation depths, of up to ∼4 Å in the current study, before they reached a constant value. Contacts with various indenter sizes showed the same trend, except for the contacts with the indenter radii of 15 Å and 20 Å: these two contacts were different due to their stepped-like increment in the number of interacting atoms. Moreover, it was shown that the contact distance is a function of the indenter's radius, in the form of $d_c \cong 4R^{0.05}$. It should be noted that the results may be different for different systems: in other words, the results could be affected by changing the material, temperature, crystallographic orientation, applied potential energies, and indentation velocity.

Furthermore, the contact behaviors of two different types of rough surfaces, a multi-asperity GW-type rough surface and a comparable random one, were investigated. The contact behaviors of both systems were found to be very close. Moreover, the results of the present study show that the relative projected contact area is a linear function of nominal pressure, even after plastic deformation is initiated locally.

The multi-asperity rough surface was studied by the GW theory, and it was found that using the elastic contact modulus of $E^* = 28.57$ GPa, the theory overestimates the contact area of the simulated system. Furthermore, both, the GW and Persson theories were used for studying the contact behavior of the randomly rough surface. The results show that the estimation of the contact area in the Persson theory is highly dependent on the method used to calculate the parameter G: the theory would correctly describe the contact behavior if G were calculated using its theoretical solution in Eq. (7), or as the fitting parameter of Eq. (8); however, calculation of $G = \frac{1}{8}E^{*2}\langle|\nabla h|^2\rangle$ results in some inconsistency of the length scale, which would be problematic, at least for studying atomistic systems.

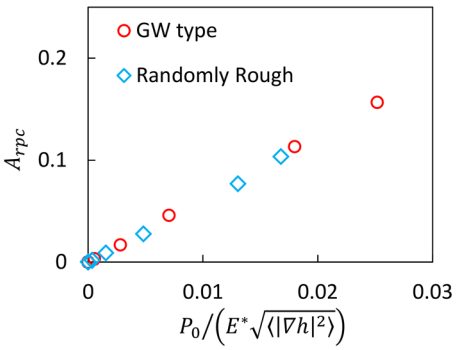

FIG. 22. The relative projected contact area as a function of normalized pressure for both of the simulated systems with rough surface contacts.

ACKNOWLEDGMENTS

The authors would like to warmly thank Professors Martin Müser of Saarland University, as well as Michele Ciavarella and Giuseppe Carbone from the Politecnico di Bari for very useful discussions and feedback during the preparation of this manuscript.

APPENDIX A: THE ATOMIC DIAMETER OF CALCIUM

The procedure for the estimation of the atomic diameter of a single calcium atom is explained in this Appendix. In classical MD simulations, the atoms are considered as spheres. Therefore, a definition for the atomic diameter is inevitable and must be used for visualization purposes. It is shown that, for a particulate system where the particles are represented as spheres with a constant diameter d_a, the diameter of the particles can be defined as the distance where two particles have the highest probability of being in contact, i.e., the first peak of the $g(r)$ plots (d_{fp}).[12] Following the method described in Ref. 12, the required $g(r)$ plot was calculated from the simulation of the NPT ensemble at zero external pressure and $T = 300$ K for a system governed by the EAM potential. As shown in Figure 23, the results suggest an atomic diameter of 3.94 Å.

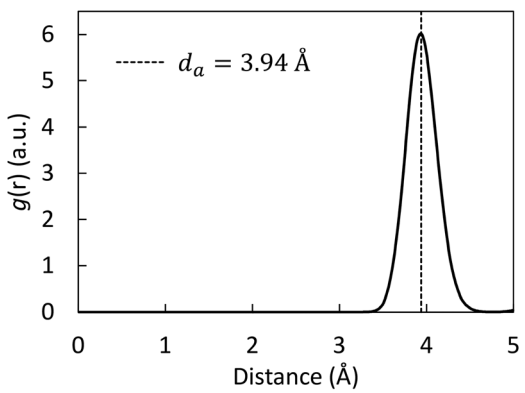

FIG. 23. The $g(r)$ plot the NPT ensemble for calcium with the EAM potential at 300 K, and under an external pressure of 0 GPa.

TABLE VI. The representation of the atomic structures of the contacting systems (normal to the x axis), and their contact-induced stress fields. The atoms are represented in the left column as circles with different colors: fixed (blue), thermostatic (red), non-constrained (green), and the indenter as white. The right column shows the projection of the maximum values of the contact influenced stress (CS) values on a plane normal to the x axis: dark blue indicates the minimum of value of 0, and dark red indicates the maximum of the values, which was 0.9 GPa, 8.5 GPa, and 10.2 GPa, for the cases of single asperity, GW rough surface, and random rough surface, respectively.

	Atomic structure	Contact induced stress field
Single asperity (1000 Å)	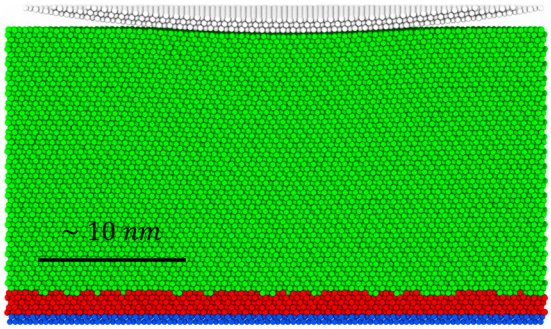	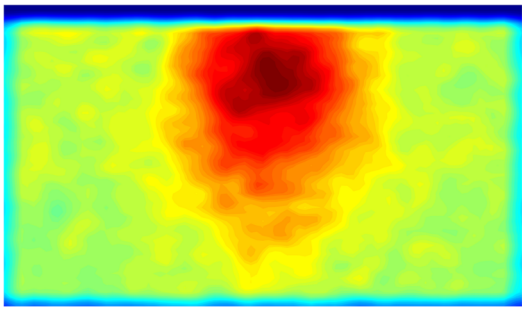
GW rough surface	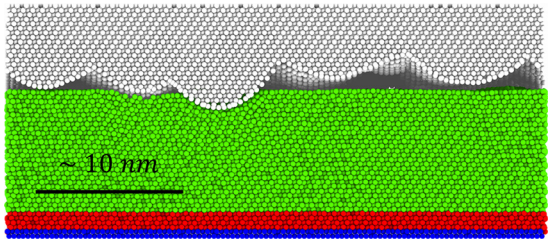	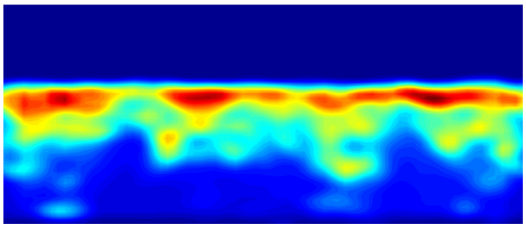
Random rough surface	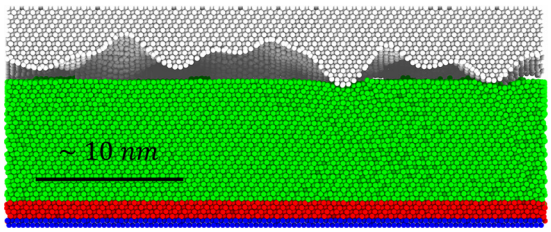	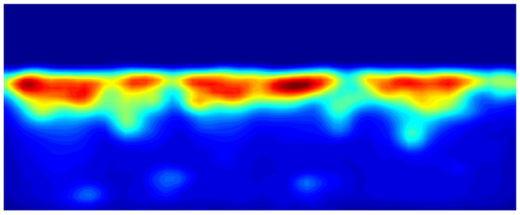

APPENDIX B: CONTACT-INDUCED STRESS FIELDS

Applying periodic boundary conditions (PBCs) along the desired directions is a classical method in MD simulations used for avoiding the edges imposed by the finite size of the simulated system. In some systems, however, such as the ones investigated in this work, PBCs are not applicable in the directions normal to a free surface. Consequently, the system's behavior, including its mechanical response, could be affected by the finite system size in the directions where PBCs are not applied.

In the current study, an atomistic fixed layer providing the necessary mechanical support to the deformable bodies was used along the plane parallel to the free surface. As a result, the mechanical response of the systems would be affected by that fixed layer if the stress fields crossed the deformable body and reached the fixed layer. Allowing for this behavior could be relevant for thin layers, but not for bulk materials as was intended in this work. In order to remove this boundary effect, one may simulate the system using Green's function MD (GFMD),[43] smartblock MD,[21] or by coupling MD with other techniques such as the finite element method (FEM), e.g., via the Atoms-to-Continuum package of LAMMPS; given sufficient computational resources, it is also possible to simulate an extremely large system using classical MD.[44] In this work, classical MD was used, and the results were collected up to the point before which the stress fields were affected by the fixed layer. This condition was tested through the calculation of the contact influenced stress values (CS) by subtracting the stress values of each atom at the end of the equilibration process (S_{eq}) from their corresponding value at each time step (S_t), i.e., $CS_t = S_t - S_{eq}$, where CS_t indicates the values of CS at time step t. Then, the system was meshed along one of the lateral axes, and the maximum values of CS were collected. By examining these data, it was possible to identify the instances at which the stress fields reached the fixed layers. Table VI shows the stress fields of a number of the contacting systems, at the last step of data extraction. Interestingly, the zone of maximum stress for the sphere-on-flat contact is localized at 33 ± 10 Å below the surface; this corresponds well to the continuum definitions of the maximum sub-surface shear stress occurring at $\sim 0.482 r_c = 43$ Å for a system with $\nu = 0.3$, where the contact patch radius r_c is ~89 Å.

[1]M. K. Yeo and Y. H. Jang, "Molecular dynamics simulation of a nanoscale sliding layer system," Wear **269**, 206–212 (2010).
[2]P. Spijker, G. Anciaux, and J.-F. Molinari, "Dry sliding contact between rough surfaces at the atomistic scale," Tribol. Lett. **44**, 279–285 (2011).

[3]X. Zheng, H. Zhu, A. Kiet Tieu, and B. Kosasih, "A molecular dynamics simulation of 3D rough lubricated contact," Tribol. Int. **67**, 217–221 (2013).
[4]S. Solhjoo and A. I. Vakis, "Molecular dynamics simulations of rough contact with fractal and statistical surface generation," in *Proceedings of the 12th Biennial Conference on Engineering Systems Design and Analysis* (American Society of Mechanical Engineers, 2014), p. V003T014A002.
[5]S. Solhjoo and A. I. Vakis, "Normal contacts of lubricated fractal rough surfaces at the atomic scale," in *Proceedings of the TriboUK* (Loughborough University, 2015), p. 36.
[6]S. Solhjoo and A. I. Vakis, "Lubricated normal and sliding contact of fractal rough surfaces at the atomic scale," in Proceedings of the International Conference on Understanding and Controlling Nano and Mesoscale Friction (2015), p. 46.
[7]K. L. Johnson, K. Kendall, and A. D. Roberts, "Surface energy and the contact of elastic solids," Proc. R. Soc. London, Ser. A **324**, 301–313 (1971).
[8]R. W. Carpick, N. Agrait, D. F. Ogletree, and M. Salmeron, "Measurement of interfacial shear (friction) with an ultrahigh vacuum atomic force microscope," J. Vac. Sci. Technol. B **14**, 1289–1295 (1996).
[9]S. Eder, A. Vernes, G. Vorlaufer, and G. Betz, "Molecular dynamics simulations of mixed lubrication with smooth particle post-processing," J. Phys.-Condens. Matter **23**, 175004 (2011).
[10]B. Luan and M. O. Robbins, "The breakdown of continuum models for mechanical contacts," Nature **435**, 929–932 (2005).
[11]Y. Mo, K. T. Turner, and I. Szlufarska, "Friction laws at the nanoscale," Nature **457**, 1116–1119 (2009).
[12]S. Solhjoo and A. I. Vakis, "Definition and detection of contact in atomistic simulations," Comput. Mater. Sci. **109**, 172–182 (2015).
[13]K. L. Johnson, *Contact Mechanics* (Cambridge University Press, 1987).
[14]H. Hertz, "Über die Berührung fester elastischer Körper," J. Reine Angew. Math. **92**, 156–171 (1881).
[15]B. V. Derjaguin, V. M. Muller, and Y. P. Toporov, "Effect of contact deformations on the adhesion of particles," J. Colloids Interface Sci. **53**, 314–326 (1975).
[16]J. A. Greenwood and J. B. P. Williamson, "Contact of nominally flat surfaces," Proc. R. Soc. London, Ser. A **295**, 300–319 (1966).
[17]B. N. J. Persson, "Elastoplastic contact between randomly rough surfaces," Phys. Rev. Lett. **87**, 116101 (2001).
[18]B. N. J. Persson, "Theory of rubber friction and contact mechanics," J. Chem. Phys. **115**, 3840–3861 (2001).
[19]M. H. Müser and W. B. Dapp, "The contact mechanics challenge: Problem definition," preprint arXiv:1512.02403.
[20]E. Gnecco and E. Meyer, "Rough contacts," in *Elements of Friction Theory and Nanotribology* (Cambridge University Press, Cambridge, 2015), pp. 75–89.
[21]C. Yang, U. Tartaglino, and B. N. J. Persson, "A multiscale molecular dynamics approach to contact mechanics," Eur. Phys. J. E **19**, 47–58 (2006).
[22]V. A. Yastrebov, G. Anciaux, and J.-F. Molinari, "From infinitesimal to full contact between rough surfaces: Evolution of the contact area," Int. J. Solids Struct. **52**, 83–102 (2015).
[23]A. P. Rigazzi, "The effects of roughness on the area of contact and on the elastostatic friction," Ph.D. thesis (Università della Svizzera Italiana, 2014).
[24]C. Yang and B. N. J. Persson, "Molecular dynamics study of contact mechanics: Contact area and interfacial separation from small to full contact," Phys. Rev. Lett. **100**, 024303 (2008).
[25]S. Plimpton, "Fast parallel algorithms for short-range molecular dynamics," J. Comput. Phys. **117**, 1–19 (1995).
[26]S. Solhjoo, A. Simchi, and H. Aashuri, "Molecular dynamics simulation of melting, solidification and remelting processes of aluminum," Iran. J. Sci. Technol.-Trans. Mech. Eng. **36**, 13–23 (2012).
[27]W. C. Swope, H. C. Andersen, P. H. Berens, and K. R. Wilson, "A computer simulation method for the calculation of equilibrium constants for the formation of physical clusters of molecules: Application to small water clusters," J. Chem. Phys. **76**, 637–649 (1982).
[28]H. J. C. Berendsen, J. P. M. Postma, W. F. van Gunsteren, A. DiNola, and J. R. Haak, "Molecular dynamics with coupling to an external bath," J. Chem. Phys. **81**, 3684–3690 (1984).
[29]S. Cheng and M. O. Robbins, "Defining contact at the atomic scale," Tribol. Lett. **39**, 329–348 (2010).
[30]A. Stukowski, "Visualization and analysis of atomistic simulation data with OVITO–the Open Visualization Tool," Modell. Simul. Mater. Sci. Eng. **18**, 015012 (2010).
[31]C. A. Schneider, W. S. Rasband, and K. W. Eliceiri, "NIH Image to ImageJ: 25 years of image analysis," Nature Methods **9**, 671–675 (2012).
[32]H. W. Sheng, M. J. Kramer, A. Cadien, T. Fujita, and M. W. Chen, "Highly optimized embedded-atom-method potentials for fourteen fcc metals," Phys. Rev. B **83**, 134118 (2011).
[33]M. S. Daw and M. I. Baskes, "Embedded-atom method - derivation and application to impurities, surfaces, and other defects in metals," Phys. Rev. B **29**, 6443–6453 (1984).
[34]J. E. Jones, "On the determination of molecular fields. II. From the equation of state of a gas," Proc. R. Soc. London, Ser. A **106**, 463–477 (1924).
[35]Z. Shu and G. J. Davies, "Calculation of the lennard-jones n-m potential-energy parameters for metals," Phys. Status Solidi A **78**, 595–605 (1983).
[36]B. R. Brooks, R. E. Bruccoleri, B. D. Olafson, D. J. States, S. Swaminathan, and M. Karplus, "CHARMM - A program for macromolecular energy, minimization, and dynamics calculations," J. Comput. Chem. **4**, 187–217 (1983).
[37]S. Solhjoo and A. I. Vakis, "Single asperity nanocontacts: Comparison between molecular dynamics simulations and continuum mechanics models," Comput. Mater. Sci. **99**, 209–220 (2015).
[38]D. Bergstrom, J. Powell, and A. F. H. Kaplan, "The absorption of light by rough metal surfaces - A three-dimensional ray-tracing analysis," J. Appl. Phys. **103**, 103515 (2008).
[39]M. Yaghoobi and G. Z. Voyiadjis, "Atomistic simulation of size effects in single-crystalline metals of confined volumes during nanoindentation," Comput. Mater. Sci. **111**, 64–73 (2016).
[40]K. Xiong, H. M. Lu, and J. F. Gu, "Atomistic simulations of the nanoindentation-induced incipient plasticity in Ni3Al crystal," Comput. Mater. Sci. **115**, 214–226 (2016).
[41]B. N. J. Persson, O. Albohr, U. Tartaglino, A. I. Volokitin, and E. Tosatti, "On the nature of surface roughness with application to contact mechanics, sealing, rubber friction and adhesion," J. Phys.-Condens. Matter **17**, R1–R62 (2005).
[42]S. Hyun, L. Pei, J. F. Molinari, and M. O. Robbins, "Finite-element analysis of contact between elastic self-affine surfaces," Phys. Rev. E **70**, 026117 (2004).
[43]C. Campañá and M. H. Müser, "Practical Green's function approach to the simulation of elastic semi-infinite solids," Phys. Rev. B **74**, 075420 (2006).
[44]A. V. Verkhovtsev, A. V. Yakubovich, G. B. Sushko, M. Hanauske, and A. V. Solov'yov, "Molecular dynamics simulations of the nanoindentation process of titanium crystal," Comput. Mater. Sci. **76**, 20–26 (2013).